THE JOURNAL OF PHYSICAL CHEMISTRY C

Article

pubs.acs.org/JPCC

Charging Rate Dependence of Ion Migration and Stagnation in Ionic-Liquid-Filled Carbon Nanopores

Alexander J. Pak and Gyeong S. Hwang*

McKetta Department of Chemical Engineering, University of Texas, Austin, Texas 78712, United States

Supporting Information

ABSTRACT: Over the past decade, interest in leveraging subnanometer pores for improved capacitance in electrochemical double layer capacitors (EDLCs) has readily grown. Correspondingly, many theoretical studies have endeavored to understand the mechanisms that dictate the capacitance enhancement once ions are confined within nanopores, typically within quasi-equilibrium conditions. However, a kinetic-based understanding of the capacitance may be important, especially since the dynamics of ion transport can exhibit dramatic differences under confinement compared to the bulk liquid phase; ion transport is driven by the competition between the electrostatic electrode−ion and ion−ion interactions, which can be comparable as the internal surface area to volume ratio increases. In this work, we study the relationship between the dynamics of 1-ethyl-3-methylimidazolium tetrafluoroborate (EMIM/BF_4) ionic liquid and the capacitance within two idealized cylindrical subnanometer pores with diameters of 0.81 and 1.22 nm using classical molecular dynamics simulations. By adjusting the voltage scan rate, we find that the capacitance is highly sensitive to the formation of an electroneutral ionic liquid region; with rapid charging, consolidated anion−cation contact pairs, which remain trapped within the pore, restrict the local accumulation of charge carriers and, thereby, the capacitance. These findings highlight potential kinetic limitations that can mitigate the benefits from electrodes with subnanometer pores.

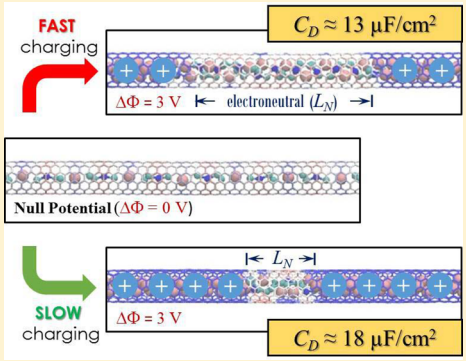

INTRODUCTION

Supercapacitors, also referred to as electrochemical double layer capacitors (EDLCs), are energy storage devices known for their characteristically large power densities (i.e., charge/discharge occurs within seconds) and long lifetimes (over hundreds of thousands of cycles).[1−3] The source of these properties is related to the fundamental operating mechanism of these devices; injected charge carriers are stored by the formation of the so-called electric double layer (EDL), which consists of the electrode surface charge electrostatically balanced by the accumulation of electrolyte counterions at the interface. Applications of EDLCs, however, are limited by their intrinsically low energy densities. As the energy density ($E = {}^1/_2CV^2$) is proportional to the capacitance (C) and the square of the operating voltage (V), researchers have been interested in finding new electrode and electrolyte materials that can increase both C and V.

The search for electrode materials has conventionally been directed toward finding materials with good electrical conductivity and specific surface areas larger than commercially used activated carbons.[1−3] For these reasons, carbon nanomaterials, including graphene, carbon nanotubes (CNTs), and carbide-derived carbons (CDCs), have all been recent subjects of interest. However, the work of Chmiola and co-workers,[4] and later Largeot and co-workers,[5] showed that the areal C (i.e., C normalized to surface area) can exhibit dramatic improvement by tuning the average pore width, in CDC electrodes, to be comparable to the size of the counterion. These studies suggest that beyond maximizing the surface area, controlling the pore size distribution offers a new way of increasing C. Exploring this materials development route, however, requires that we understand the atomistic nature of charge storage when ions are confined in nanopores.

The mechanisms responsible for the enhancement in C have been the subject of several theoretical studies; in these works, the electrode is commonly modeled as idealized slit nanopores. A simple phenomenological model theorized that polarizable electrode walls screen long-range electrostatics to allow tight packing of counterions (i.e., the constituent ions that are used to compensate the electrode surface charge) in a so-called superionic state.[6] Classical molecular dynamics (MD) simulations demonstrated consistent behavior, in which confined counterions were found to maintain elevated density within the charged nanopores while co-ions (i.e., the constituent ions with charges opposite to that of the counterions) were expelled.[7] Several additional factors have been identified as possible ways of tuning C. For example, an oscillatory dependence of C based on the pore size was revealed by both classical MD[8] and classical density functional theory (DFT)[9] simulations, which was attributed to interference from overlapping EDLs. In

Received: July 2, 2016
Revised: October 12, 2016
Published: October 17, 2016

DOI: 10.1021/acs.jpcc.6b06637
J. Phys. Chem. C 2016, 120, 24560−24567

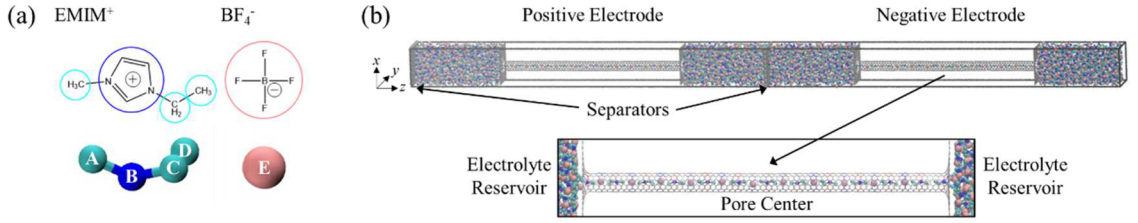

Figure 1. (a) Schematic of the $EMIM^+/BF_4^-$ ionic liquid studied in this work. Each ion is coarse-grained such that a group of atoms (circled) are modeled as a single interaction site. In particular, the $EMIM^+$ cation is modeled using four interaction centers (shown by the cyan and blue balls labeled A–D) while the BF_4^- anion is modeled using a single interaction center (shown by the pink ball labeled E). (b) Schematic of the simulation domain (periodic in all three directions) consisting of two 16 nm CNT electrodes (shown by gray lines) immersed in ionic liquid (shown by the cyan, blue, and pink balls). The length of the simulation domain is 64 nm in the z direction. The two walls of gray balls represent graphene sheets which separate the two electrode domains.

addition to the pore size dependence, classical MD simulations showed that C can be dependent on V and may be maximized when the co-ions were fully expelled before the need for additional counterion insertion.[10]

Beyond slit-pore geometries, limited studies have investigated other subnanometer pore geometries despite theoretical evidence of greater charge storage in increasingly confined regions.[11] Ions confined within cylindrical nanopores, such as CNTs, constitute one such extreme case. In the absence of external potential, several experimental studies have investigated the structure of ILs in CNTs with diameters less than 3 nm, which report the adoption of a solidlike phase.[12,13] Using constant-charge MD simulations, in which the excess electrode charge is fixed and uniformly distributed, distinct ordering of ILs both axially and radially was also predicted in charged CNTs.[14] However, it may be important for molecular simulations of ILs confined within nanopores to transition toward equipotential descriptions of the electrode, rather than the commonly used constant charge approximation. For example, recent Monte Carlo simulations have demonstrated the use of induced image charges to investigate the capacitance of ions confined within cylindrical nanopores.[15,16] Within the limited volume of such nanopores, we might also expect cations and anions to be segregated, which can subsequently induce a surface charge redistribution. To explore the kinetics of such systems, constant potential methods within a molecular dynamics framework can be beneficial.

As the primary incentive for supercapacitor adoption is their excellent power capabilities, the dynamics of ions confined in charged nanopores are also important to fully understand. This is particularly relevant for ionic liquid (IL) electrolytes, which are solvent-free ions that typically remain in the liquid phase at room temperature; IL electrolytes have been widely explored due to their large electrochemical windows that range up to 4 V. In the bulk liquid phase, ILs are known to have high viscosities due to strong ion–ion interactions,[17] which can further increase under confinement.[18] Yet interestingly, molecular simulations suggest that the self-diffusivities of these ions can exceed that of the bulk fluid when confined within charged pores with sufficiently narrow widths and large potentials.[19,20]

In the case of supercapacitors, further insights can be gleaned from the relative transport of counterions and co-ions. For example, a nonequilibrium MD study recently suggested that capacitive performance during rapid charging/discharging (i.e., large scan rate) is governed almost solely by the migration of counterions into/out of nanoslit pores.[21] In addition, recent experiments using the electrochemical quartz crystal microbalance method have demonstrated that co-ions within CDCs can be almost completely excluded at large potentials yet remain present at small potentials.[22,23] Both of these observations likely pertain to two competing driving forces for ion transport. The first is the externally applied force associated with the electrostatic attraction (repulsion) between the electrode surface and counterions (co-ions). The second is the electrostatic force between ions that can facilitate ion association, or contact pairs, between counterions and co-ions, which can conceivably counteract the aforementioned electrode/co-ion repulsive forces; this is especially true in the absence of solvent, such as in neat ILs, as the electrostatic force between ions is unmitigated.

In this study, we investigate the mechanism and dynamics of charge storage for 1-ethyl-3-methylimidazolium ($EMIM^+$) tetrafluoroborate (BF_4^-) IL in cylindrical nanopores; the electrodes are modeled as CNTs under equipotential constraints, and the IL ions are simulated using classical MD. Our specific interest is to study the influence of extreme confinement and external bias on the reorganization and migration of IL ions and, subsequently, the capacitance; we consider pore diameters (D_p) that are comparable to the size of a single ion in order to probe the competition between the electrostatic ion–electrode and ion–ion interactions. Upon charging, we observe filling of the pore by excess counterions from adjacent electrolyte reservoirs while co-ions are expelled as cation/anion contact pairs. However, we find that the capacitance is strongly dependent on the degree of co-ion expulsion; IL contact pairs that remain within the pore tend to aggregate to form electroneutral segments of IL that inhibit local accumulation of injected charge carriers and suppress the capacitance. Our analysis further demonstrates that this behavior can be modulated by the potential scan rate ($= \Delta\Phi/\tau_{chg}$) based on the applied full-cell potential ($\Delta\Phi$) and the charging time (τ_{chg}). These findings can provide a framework to investigate kinetic limitations of capacitive storage in subnanometer pores.

RESULTS AND DISCUSSION

Simulation Framework. We consider a simulation domain that emulates a two-cell EDLC filled with $EMIM^+/BF_4^-$ ions, as depicted in Figure 1, which are modeled using a coarse-grain force field (see Methods section). The electrodes are armchair CNTs grafted onto graphene sheets such that ions can only fill the inside of the pore. Additional graphene sheets are included to separate the positive and negative electrode domains, such that the total number of cations/anions is equivalent within each domain, or the so-called half-cell (see Supporting

DOI: 10.1021/acs.jpcc.6b06637
J. Phys. Chem. C 2016, 120, 24560–24567

Information for additional details). We introduce a fluctuating charge model for the electrodes adapted from the charge equilibration (Qeq) scheme[24] (see Methods section) to reproduce constant potential surfaces with $\Delta\Phi = \Phi_{pos} - \Phi_{neg}$, which are the respective surface potentials of the positive and negative electrodes. In the following sections, we first investigate the relationship between the electrode charge density and ion density distributions in two different electrodes with D_p = 0.81 and 1.22 nm when $\Delta\Phi$ is both neutral and charged. We then evaluate the capacitance as a function of potential scan rate, which we decouple in terms of applied full-cell potential ($\Delta\Phi$) and charging time (τ_{chg}), and relate these observations to the structure of the confined IL. Finally, we perform nonequilibrium MD simulations to explore the transient IL and electrode charge redistribution during charging.

Ionic Liquid and Electrode Charge Distributions within Neutral Electrodes. We first investigate the electrode charge density (σ_{CNT}) and ionic liquid (IL) number density (ρ_{ion}) distributions under zero applied bias ($\Delta\Phi$ = 0 V). Two CNT electrodes with D_p = 0.81 and 1.22 nm are considered with a length (L_p) of 16 nm to maintain large aspect ratios and remove possible entrance effects ($L_p \gg D_p$ or $L_p/D_p > 10$).

Figure 2a depicts a snapshot of the ions confined within the positive electrode. When D_p = 0.81 nm, the ions are observed to form a molecular wire structure with highly partitioned cations and anions. As such, distinct peaks are seen to alternate between cations and anions in the ρ_{ion} plots shown in Figure 2b, in agreement with observations with previous computational work.[14] Here, only a single ion can be accommodated radially as the effective van der Waals (vdW) diameter of the cation (anion) interacting with graphitic carbon is modeled as 0.78 (0.76) nm, which is slightly smaller than D_p and effectively limits the ability of ions to pass over other ions during axial transport. In contrast, when D_p = 1.22 nm, the comparatively larger internal volume allows the ions to mix axially, albeit in a spiral-like configuration; the removal of axial segregation is evident by the suppressed oscillations in the ρ_{ion} profile shown in Figure 2c. The $EMIM^+$ cations also tend to conform close to the electrode walls (Figure 2a) as this configuration maximizes both the interfacial vdW and electrostatic interactions. Note that in both cases the average total ρ_{ion} is nearly 4 ion/nm^3; for comparison, the ρ_{ion} in the bulk is around 8 ion/nm^3.

To maintain charge neutrality throughout the electrode region, the charge of each ion should be compensated by the neighboring environment, which considers both adjacent ions and the local electrode charge. Because of the single-wire configuration of ions when D_p = 0.81 nm, the ionic contribution to screening only occurs in the axial direction. Significant charge puddling along the electrode surface, as seen by the large oscillations in the σ_{CNT} plot shown in Figure 2d, is therefore induced to additionally screen the ionic charge; for example, the electrode surface near cations (anions) is noticeably electron accumulating (depleting). However, in the D_p = 1.22 nm case, the absence of distinct cation−anion segregation in the axial direction also mitigates the extent of charge puddling along the CNT surface (Figure 2d). Note that in both cases the charge inhomogeneity is necessary to maintain a constant electrode surface potential.

Ionic Liquid and Electrode Charge Distributions within Charged Nanopores. Next, $\Delta\Phi$ = 3 V is impulsively applied to the electrodes. In our simulations, the electrodes are allowed to equilibrate for 4 ns before statistics are extracted

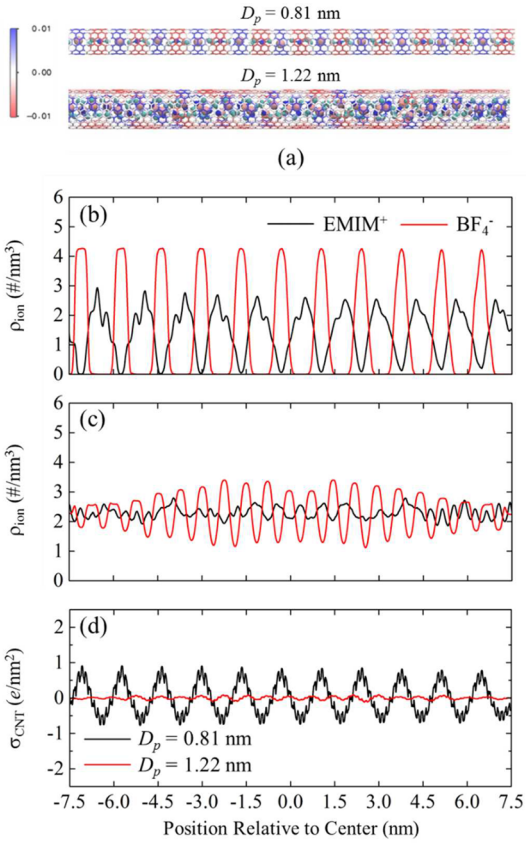

Figure 2. (a) Snapshot of the ions confined within the neutral CNT electrodes with the charge per carbon atom (in e) represented as a color map (blue and red are positive and negative charge, respectively); $EMIM^+$ cations are represented as four bonded cyan balls while BF_4^- anions are represented as one pink ball. Ion number density (ρ_{ion}) profiles as a function of distance from the neutral electrode center when (b) the pore diameter D_p = 0.81 nm and (c) D_p = 1.22 nm. (d) Electrode excess surface charge density (σ_{CNT}) in the axial direction of the electrode.

over additional 2 ns trajectories. Interestingly, as depicted in Figure 3a, distinct differences in the IL structures appear when comparing the two electrode diameters. Most notably, the IL distribution along the axial direction of the positive electrode is heterogeneous when D_p = 0.81 nm and homogeneous when D_p = 1.22 nm. For simplicity, the negative electrode is not depicted but has qualitatively similar features (see Figures S1 and S2), as discussed below, with slight differences based on the cation and anion sizes.

First, let us examine the influence of D_p on ρ_{ion} once the electrodes are charged. In the more confined case (D_p = 0.81 nm), a region containing both $EMIM^+$ co-ions and BF_4^- counterions develops within the center of the positive electrode, as depicted in Figure 3a. As seen in Figure 3b, the average ρ_{ion} of both counterions and co-ions in this region is nearly equivalent (around 4 ion/nm^3), suggesting that ionic charge in the axial center region is electroneutral; hereafter, this region will be referred to as the "electroneutral" or "charge neutral" region. Beyond this electroneutral region, the inner pore of the CNT is completely populated by BF_4^- counterions. A sharp interface of highly packed anions is observed adjacent to the electroneutral region with tapering ρ_{ion} toward the two ends of the pore (Figure 3b). In contrast, the IL structure in the less confined case (D_p = 1.22 nm) appears to be comparatively

DOI: 10.1021/acs.jpcc.6b06637
J. Phys. Chem. C 2016, 120, 24560−24567

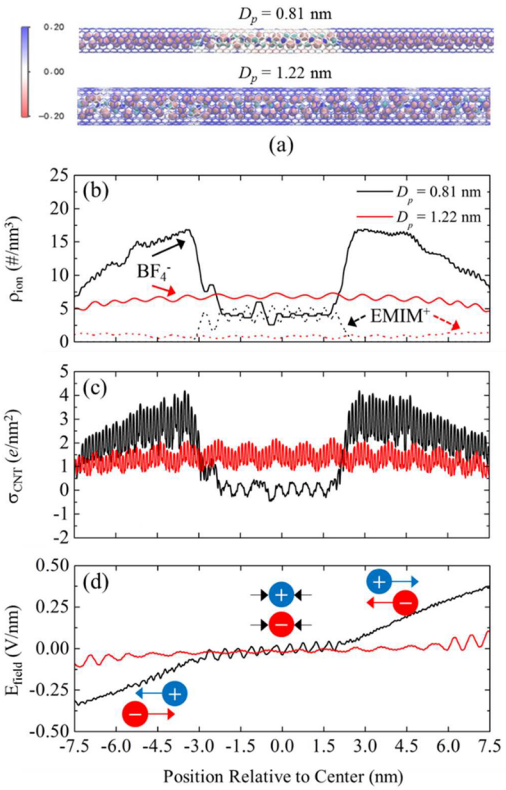

Figure 3. (a) Snapshot of the ions confined within the positive CNT electrodes when the applied full-cell potential is 3 V with the charge per carbon atom (in e) represented as a color map; $EMIM^+$ cations represented as four bonded cyan balls while BF_4^- anions represented as one pink ball. (b) Ion number density (ρ_{ion}) profiles as a function of distance from the positive electrode center. (c) The corresponding electrode excess surface charge density (σ_{CNT}) along the axial direction with (d) the computed total electric field (E_{field}) in the axial direction.

more homogeneous in the axial direction. Figure 3a shows that the BF_4^- counterions form a sheathlike structure that both screens the electrode charge and shields the molecular chain of $EMIM^+$ co-ions that forms along the axis of the pore.

Interestingly, the magnitude of the total ρ_{ion} (i.e., the sum of the cation and anion ρ_{ion}) after charging is comparable to a solidlike phase. For example, the total ρ_{ion} when D_p = 0.81 nm peaks around 16 ion/nm^3 at the aforementioned interface. In the center of the D_p = 1.22 nm case, a slight ion accumulation is also observed with total ρ_{ion} around 7 ions/nm^3. In comparison, the solid monoclinic phase of $EMIM/BF_4$ has been observed to have a total ρ_{ion} of 8.6 ions/nm^3 at 173 K.[25] Here, the larger ρ_{ion} in the case of the narrower pore can be attributed to a stronger electric field imposed by the excess charge on the electrode surface that can compensate anion−anion repulsion.

Although not shown here, the IL structures within the negative electrodes (see Figure S1) show qualitatively similar trends with subtle differences based on the shapes/sizes of the cations and anions. With negative polarization, $EMIM^+$ cations become counterions that are notably bulkier than the spherical and compact BF_4^- anions. One consequence is that the ρ_{ion} of the counterion tends to be reduced; when D_p = 0.81 nm, the maximum ρ_{ion} is around 6 ions/nm^3 (compared to 16 ions/nm^3 in the positive electrode), which is likely due to the bulkiness of the cation both facilitating the screening of the electrode charge and restricting ion packing due to steric hindrance (Figure S1a). In addition, a larger number of co-ions can be trapped, as seen in the D_p = 1.22 nm case (Figure S1b), as the bulkier $EMIM^+$ counterions may serve as a greater steric barrier than BF_4^- counterions in the positive electrode. In this case, the $EMIM^+$ counterions nonetheless form an effective sheath separating the polarized electrode and the trapped co-ions.

Next, we consider the σ_{CNT} profiles. Similar to the neutral case, the σ_{CNT} profiles when $\Delta\Phi$ = 3 V closely resemble the IL structure. As a result, σ_{CNT} is highly nonuniform when D_p = 0.81 nm and appears uniform when D_p = 1.22 nm, as seen in Figure 3c. The latter case, for example, exhibits a nearly flat profile in the axial direction with slight accumulation in the center region. However, in the D_p = 0.81 nm case, the σ_{CNT} profile steadily rises from the pore ends toward the center, which is commensurate with the increasing counterion ρ_{ion}, before abruptly diminishing to neutral charge in the center region; recall that the ions in this region are electroneutral due to trapped co-ions. This suggests that injected charge carriers tend to accumulate outside of the electroneutral region; here, the length of the electroneutral region (L_N) is 4.1 nm as seen in Figure 3b,c.

Finally, from the computed ionic and electrode charge densities, the electric field (E_{field}) in the axial direction is calculated using Poisson's equation in 1D (see Supporting Information) and shown in Figure 3d. First, it is noteworthy that although the electrode surface maintains a constant potential, a transaxial potential and E_{field} can develop due to an ionic concentration gradient along the pore axis. In fact, it is this potential gradient that can drive counterions into the pore and co-ions out of the pore. In addition, the magnitude of E_{field} is much larger in the D_p = 0.81 nm case, owing to the greater ion packing density and segregation, suggesting that the field-driven ion transport can also be faster. Yet despite this large driving force for the inward migration of counterions, it appears that a steric barrier prevents the counterions from penetrating into the electroneutral region.

Influence of Applied Potential and Charging Rate on Capacitance. Now, the double layer capacitances ($C_D = 2q_{elec}/(S\Delta\Phi)$) are computed based on $\Delta\Phi$ and the total charge (q_{elec}) and surface area (S) of a single electrode; here, $\Delta\Phi$ is varied between 0.25 and 3 V. Note that in two-electrode experiments and in our simulations the half-cell potential is not strictly controlled. Hence, the factor of 2 is used to approximate the half-cell potential. However, we can expect the potential drop to be slightly larger at the positive half-cell given the denser accumulation of counterions; indeed, the calculated potential drops in the positive and negative half-cells are 1.9 and 1.1 V, respectively, based on the numerical solution to the three-dimensional Poisson's equation (see Supporting Information and Figure S3 for more details). Nonetheless, the aforementioned approximation to the C_D is used for simplicity.

As seen in Figure 4a, it is clear that the electrode with smaller diameter tends to have a larger C_D; for example, at $\Delta\Phi$ = 3 V, C_D is 15.1 and 13.0 μF/cm^2 for D_p = 0.81 and 1.22 nm, respectively. This is consistent with both earlier experimental[4,5] and (slit-pore) theoretical[7−9] observations that suggest that the capacitance can be enhanced with subnanometer pores; we also note that the observed C_D values here are likely larger than similar cases seen in ref 14 as constant-charge conditions can overestimate potential differences across interfaces.[26] In both electrode cases, we find that C_D diminishes with increasing $\Delta\Phi$, thereby mitigating the predicted enhancement at large $\Delta\Phi$. Previous simulations of graphene/IL interfaces reported a similar dependence of $\Delta\Phi$ on C, which is attributed to the

DOI: 10.1021/acs.jpcc.6b06637
J. Phys. Chem. C 2016, 120, 24560−24567

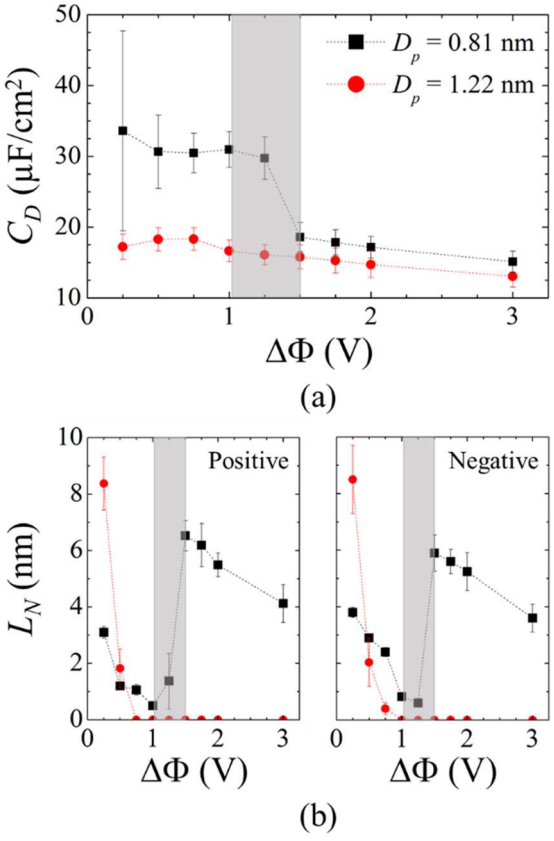

Figure 4. (a) Areal integral double-layer capacitance (C_D) with respect to the applied full-cell potential ($\Delta\Phi$) which is instantaneously applied. (b) Length of the electroneutral region (L_N) as a function of $\Delta\Phi$ at the (left) positive and (right) negative electrode. The shaded region in all panels depicts the transition between ion migration and stagnation, as discussed in the text.

increasing saturation of ions in the EDL.[27−29] In these cases, the diminishment is gradual and continuous. However, an anomalously distinct reduction (around 40−50%) of C_D is observed between $\Delta\Phi$ = 1 and 2 V in the D_p = 0.81 nm case, in contrast to the expected behavior represented in the D_p = 1.22 nm case.

To explain these observations, we assess the possible development of an electroneutral region. Figure 4b shows the computed L_N for both electrode cases on the positive and negative sides. Two distinct regimes become immediately obvious. The first is the low potential regime ($\Delta\Phi$ < 1 V) in which both D_p = 0.81 and 1.22 nm cases exhibit a reduction in L_N as $\Delta\Phi$ increases. As discussed in depth later, the L_N diminishes as more co-ions are expelled from the pore while both the electrode surface charge and excess counterions diffuse from the pore ends toward the center. However, a transition occurs around $\Delta\Phi$ = 1.25 V such that when $\Delta\Phi$ > 1.5 V, L_N abruptly increases in the D_p = 0.81 nm case before gradually decreasing with increasing $\Delta\Phi$. Here, the large density of counterions entering the pore sterically prevents co-ion expulsion, such that an electroneutral region forms within the center of the pore; as seen in Figure S3a,b, the presence of the electroneutral region can reduce the total amount of injected charge at a given applied potential. While similar behavior is seen in the D_p = 1.22 nm case, the pore remains large enough for the counterions to screen the interaction between the trapped co-ions and electrode wall. Nonetheless, both electrode cases exhibit a transition between co-ions migrating out of the pore and co-ions remaining inside the pore, which seems to depend on the rate of counterion insertion into the pore.

Comparing the positive to negative electrodes, the trend in L_N appears to be qualitatively similar. The major difference is that in the latter case L_N tends to be larger than the former case when $\Delta\Phi$ < 1 V and smaller when $\Delta\Phi$ > 1.5 V. This is likely related to the difference in the counterion size. In the low potential regime ($\Delta\Phi$ < 1 V), the bulky $EMIM^+$ counterion in the negative electrode can screen the electrode charge more efficiently than the compact BF_4^- counterion in the positive electrode; as the injected charge tend to diffuse from the pore ends toward the center in this regime, this size difference explains the observation of a larger L_N. By the same argument, the bulkiness of the $EMIM^+$ counterion compared to the compact BF_4^- co-ion may also facilitate the compression of the electroneutral region in the high potential regime ($\Delta\Phi$ > 1.5 V), thereby resulting in a smaller L_N.

Given that the formation of the charge neutral region is dependent on ion migration kinetics, we also investigate the influence of τ_{chg} by linearly varying $\Delta\Phi$ from 0 to 3 V over τ_{chg} (or scan rate = $\Delta\Phi/\tau_{chg}$), after which the system is allowed to equilibrate for 2 ns. Figure 5 shows the computed C_D and L_N as

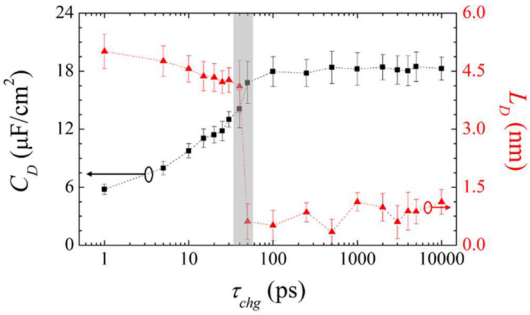

Figure 5. Influence of charging time (τ_{chg}) on (left) the double-layer capacitance (C_D in black squares) and (right) length of the electroneutral region (L_N in red triangles) at the positive electrode with diameter 0.81 nm when the applied full-cell potential is 3 V. The shaded region depicts the transition between ion migration and stagnation, as discussed in the text. The two arrows (and circles) indicate the axis that is associated with the plotted data set.

a function of τ_{chg} when D_p = 0.81 nm. At fast scan rates (τ_{chg} < 40 ps), C_D dramatically decreases with decreasing τ_{chg}. Here, we find that the suppression in C_D is commensurate with a larger L_N that can be as large as 30% of the pore length, making that region inaccessible for charge storage. However, an abrupt change in both C_D and L_N is predicted when τ_{chg} > 40 ps. At these slower scan rates, C_D saturates to around 18 $\mu F/cm^2$ while L_N is less than 1.5 nm (<10% of the pore length). Note that even at a large τ_{chg} of 10 ns, some co-ions remain trapped within the pore; this is likely due to the strong electrostatic attraction between co-ions and counterions which can inhibit complete segregation. Nonetheless, these results suggest that the capacitance of these subnanometer pore electrodes can be nonlinearly sensitive to the scan rate (= $\Delta\Phi/\tau_{chg}$), which determines if co-ions (and their contact-paired counterions) can be expelled from the pore.

E. Transient Migration of Ions during Charging. To understand the molecular origins of the observed transition between co-ion expulsion and stagnation, we investigate the behavior of the electrolyte ions and electrode charge as a

DOI: 10.1021/acs.jpcc.6b06637
J. Phys. Chem. C 2016, 120, 24560−24567

function of elapsed time (t) throughout the pore with D_p = 0.81 nm after $\Delta\Phi$ is impulsively applied.

In Figure 6, we compare the total sum of ions (n_{ion}) and electrode charge (q_{elec}) within the positive electrode as a function of t for a broad range of $\Delta\Phi$ (see Table S1 for summarized data). Observation of the n_{ion} profiles (Figure 6a) shows a noticeable difference between the low-potential ($\Delta\Phi$ < 1 V) and high-potential ($\Delta\Phi$ > 1.5 V) regimes. For example, in the low-potential regime, n_{ion} exhibits oscillatory behavior in which n_{ion} initially increases, then decreases, and finally readily increases. This implies that excess ions initially fill the pore, followed by ion expulsion from the pore and subsequent ion refilling into the pore. On the other hand, in the high-potential regime, we find that n_{ion} initially increases before saturating, which implies that the pore only undergoes filling by excess ions. The q_{elec} profiles (Figure 6b) expectedly show consistent behavior; they increase and saturate in the high-potential regime yet exhibit notable kinks in the low-potential regime which precede the concavity changes in the n_{ion} profiles.

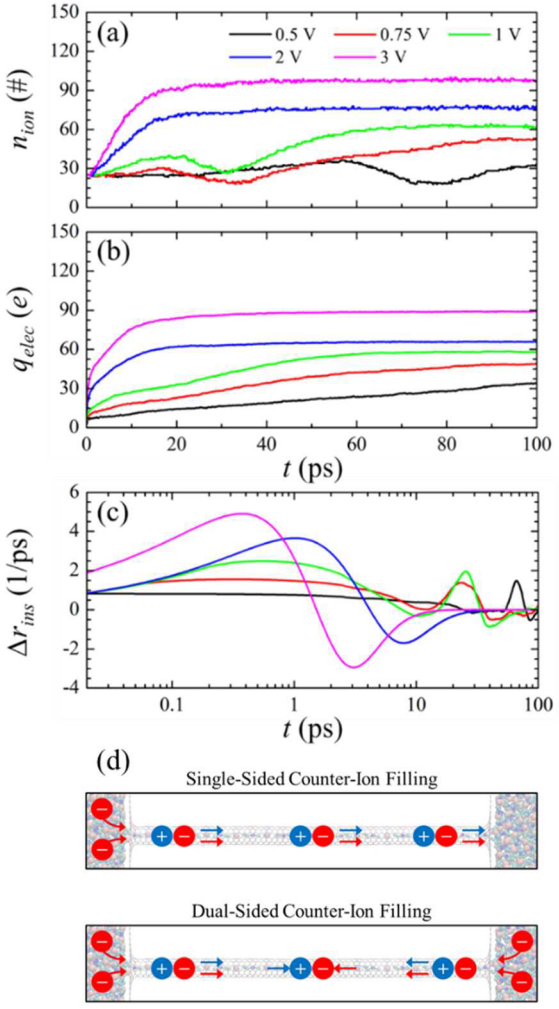

Figure 6. (a) Total number of confined ions (n_{ion}), (b) total excess surface charge (q_{elec}), and (c) the difference in the rate of electrode charge insertion and ion insertion (Δr_{ins}) within the positive electrode as a function of time (t) when the listed full-cell potential is applied starting at 0 V. (d) Schematic depicting the two counterion filling regimes as described in the text. The electrode diameter is 0.81 nm.

The major difference that separates these two potential regimes can be attributed to the competition between the migration of excess counterions (i.e., ions from outside the pore) and of co-ion/counterion contact pairs within the pore. According to a closer analysis of the $\Delta\Phi$ = 0.5 and 3 V cases (Figure S4), co-ion/counterion contact pairs are expelled from the pore when driven by the filling of excess counterions from only one side (Figure 6d). However, when excess counterions predominately fill the pore from both sides (Figure 6d), the co-ion/counterion contact pairs are instead driven toward the pore center, which eventually forms the charge neutral region.

Conceivably, this behavior is dependent on the rate of excess charge injection (= $\partial q_{elec}/\partial t$) compared to the rate of ion insertion (= $\partial n_{ion}/\partial t$). For example, the aforementioned single-sided filling (i.e., asymmetric flow) is indicative of a transaxial potential gradient, which is likely only possible at low potentials (or when a small amount of charge carriers has been injected) as the electrode charge distribution can remain significantly perturbed by the local ionic environment. Interestingly, in the low potential regime, the transition from ion contact pair expulsion to counterion filling appears to occur at increasingly lower t as $\Delta\Phi$ increases (Figure 6a), which suggests that once $\Delta\Phi$ is large enough, the field generated by the injected charge carriers dominates and drives excess counterion filling from both pore ends. To quantify the competition between the two aforementioned rates, we compute their difference (Δr_{ins} = $\partial q_{elec}/\partial t - \partial n_{ion}/\partial t$), as shown in Figure 6c.[30] We find in the $\Delta\Phi$ < 1 V cases Δr_{ins} exhibits a shallow initial increase, commensurate with single-sided counterion filling, before a secondary peak in Δr_{ins} appears that corresponds with the transition toward dual-sided counterion filling. On the other hand, Δr_{ins} increase far more rapidly in the $\Delta\Phi$ > 1.5 V cases and only exhibits a single peak before fluctuating toward zero. This further supports the importance of tuning the rate of charge carrier injection relative to the rate of ion migration to dictate the pore filling dynamics. As such, the transition point, as determined by potential scan rate (= $\Delta\Phi/\tau_{chg}$), will likely also depend on other factors including the diffusivity and size of the electrolyte ions and the length/radius of the electrode pore.

CONCLUSIONS

To summarize, we investigated the capacitance of ionic liquids confined within charged cylindrical nanopores with diameters D_p = 0.81 and 1.22 nm using classical molecular dynamics simulations. While we find that the capacitance is expectedly larger using the narrower pore, the excess charge is observed to distribute nonuniformly along the electrode surface. During charging, the smaller pore is found to develop a so-called electroneutral region in the axial center of the pore, which is formed by the aggregate of trapped co-ion/counterion contact pairs. As the accumulation of excess charge around this electroneutral region is electrostatically unfavorable, a significant fraction of the electrode cannot effectively participate in charge storage. Molecular analysis during the transient charging regime attributes the development of the electroneutral region to the rapid overfilling of counterions into the pore. In addition, the length of the electroneutral region is found to be strongly dependent on the competition between the rate of excess charge injection and ion migration, which in turn can be controlled by the potential scan rate (= applied potential/charging time). It is evident that such phenomena may be related to the experimentally observed capacitance fading at large scan rates.

DOI: 10.1021/acs.jpcc.6b06637
J. Phys. Chem. C 2016, 120, 24560−24567

While idealized electrodes were studied in this work, the methodological approach and analysis can be extended to many other factors which remain largely unexplored. One possible factor is the possible nonuniformity of the pore structure (e.g., pore dispersity based on length, radius, and shape) while another is the geometry of different ions (e.g., size, shape, flexibility, and charge distribution). Our previous work[31−33] has also suggested that different surface chemistries (e.g., chemical functionalization or impurities) can greatly influence surface charge accumulation and localization, which can also affect ion distribution and mobility throughout the pore; here, possible electrolyte decomposition within highly charged electrodes should be considered. Nonetheless, these findings highlight the importance of investigating the transition between the migration or stagnation of confined ions for the design of future nanoporous materials for supercapacitor applications.

COMPUTATIONAL METHODS

We employed classical MD simulations using LAMMPS[34] to investigate the organization and capacitance of IL molecules confined within fixed CNT electrodes. The IL molecules were described using coarse-grain parameters (Table 1) with

Table 1. Coarse-Grain Parameters Primarily from Refs 35 and 37, with q Rescaled Following the Fashion of Ref 36 and σ Reoptimized To Reproduce Experimental Density and Diffusivity

site	ε (kcal/mol)	σ (Å)	q (e)
A	0.157	3.90	0.1733
B	0.643	4.32	0.3741
C	0.141	3.90	0.1647
D	0.157	3.90	0.0679
E	0.339	4.10	−0.7800

partitioning depicted in Figure 1; $EMIM^+$ cations contained four interaction centers while BF_4^- anions contained one interaction center. The LJ parameters were adapted from ref 35; the charges (q) were rescaled following the fashion of ref 36 while the zero-energy pairwise distance (σ) were reoptimized to reproduce experimental density and diffusivity (Table S2). The bond, angle, and dihedral parameters were adopted from ref 37 with the latter case adapted for the OPLS form. The LJ parameters for the electrode carbon atoms were taken from ref 38. All LJ and Coulomb energies were calculated using a spherical cutoff radius of 16 Å with the long-range Coulomb energies included by the particle−particle particle−mesh method.[39,40] We have compared the use of this model to that of an all-atom OPLS force-field from refs 41 and 42 and find qualitatively good agreement in electrode charge and IL structure under neutral and charged conditions (Figure S5).

While the positions of the electrode atoms were fixed, the charge of each atom was allowed to fluctuate to emulate constant potential surfaces (with $\Delta\Phi$). We adapted the charge equilibration (Qeq) scheme,[24] which is commonly used in ReaxFF simulations.[43] This method is based on equalization of the electronegativity. Here, the electronegativity of the positive (negative) electrode is rigidly shifted by $-\Delta\Phi/2$ ($+\Delta\Phi/2$); while the IL charges are fixed, the electrode charges are solved iteratively at every time step with the sum of the total electrode charge constrained to zero. The short-range Coulomb interactions included shielding corrections[43] while the long-range Coulomb interactions were solved using the fast multipole method.[44] The Qeq parameters for carbon were adopted from ref 45.

The simulation domain consisted of two 16 nm CNT electrodes (grafted onto graphene) separated by 16 nm of IL for a total size of $3.45 \times 3.42 \times 64$ nm^3 with periodic boundary conditions in all three directions. When D_p = 0.81 (1.22) nm, 1580 (1680) IL pairs were included such that the bulklike IL regions maintained a density of 1.3 g/cm^3. Two graphene sheets were also included as a physical barrier between the positive and negative half-cells. The simulations were initially sparse with a length of 80 nm. Initial equilibration was run for 10 ns under the NVT ensemble with the temperature set to 700 K as controlled by the Nosé−Hoover thermostat[46] with a 1 ps damping factor (see Figure S6 for further discussion) and 2 fs time step; here, electrode charges were kept fixed at zero while the simulation domain was gradually deformed to its final size. The temperature was then reduced to 300 K, and the system was allowed to equilibrate for another 2 ns with $\Delta\Phi$ = 0 V imposed. The final equilibration and production steps followed the procedure described in the main text. All reported results were obtained from the average of four independent simulations with different initial atomic configurations.

ASSOCIATED CONTENT

Supporting Information

The Supporting Information is available free of charge on the ACS Publications website at DOI: 10.1021/acs.jpcc.6b06637.

Figures S1−S6; Tables S1 and S2 (PDF)

AUTHOR INFORMATION

Corresponding Author

*E-mail: gshwang@che.utexas.edu (G.S.H.).

Notes

The authors declare no competing financial interest.

ACKNOWLEDGMENTS

This work was supported in part by the Robert A. Welch Foundation (F-1535). We also thank the Texas Advanced Computing Center for use of their computing resources.

REFERENCES

(1) Béguin, F.; Presser, V.; Balducci, A.; Frackowiak, E. Carbons and Electrolytes for Advanced Supercapacitors. *Adv. Mater.* **2014**, *26*, 2219−2251.

(2) Wang, G.; Zhang, L.; Zhang, J. A Review of Electrode Materials for Electrochemical Supercapacitors. *Chem. Soc. Rev.* **2012**, *41*, 797−828.

(3) Simon, P.; Gogotsi, Y. Capacitive Energy Storage in Nanostructured Carbon-Electrolyte Systems. *Acc. Chem. Res.* **2012**, *46*, 1094−1103.

(4) Chmiola, J.; Yushin, G.; Gogotsi, Y.; Portet, C.; Simon, P.; Taberna, P. L. Anomalous Increase in Carbon Capacitance at Pore Sizes Less than 1 Nanometer. *Science* **2006**, *313*, 1760−1763.

(5) Largeot, C.; Portet, C.; Chmiola, J.; Taberna, P.; Gogotsi, Y.; Simon, P. Relation between the Ion Size and Pore Size for an Electric Double-Layer Capacitor. *J. Am. Chem. Soc.* **2008**, *130*, 2730−2731.

(6) Kondrat, S.; Kornyshev, A. Superionic State in Double-Layer Capacitors with Nanoporous Electrodes. *J. Phys.: Condens. Matter* **2011**, *23*, 022201.

(7) Xing, L.; Vatamanu, J.; Borodin, O.; Bedrov, D. On the Atomistic Nature of Capacitance Enhancement Generated by Ionic Liquid Electrolyte Confined in Subnanometer Pores. *J. Phys. Chem. Lett.* **2013**, *4*, 132−140.

DOI: 10.1021/acs.jpcc.6b06637
J. Phys. Chem. C 2016, 120, 24560−24567

(8) Feng, G.; Cummings, P. T. Supercapacitor Capacitance Exhibits Oscillatory Behavior as a Function of Nanopore Size. *J. Phys. Chem. Lett.* **2011**, *2*, 2859−2864.
(9) Jiang, D. E.; Jin, Z.; Wu, J. Oscillation of Capacitance inside Nanopores. *Nano Lett.* **2011**, *11*, 5373−5377.
(10) Wu, P.; Huang, J.; Meunier, V.; Sumpter, B. G.; Qiao, R. Voltage Dependent Charge Storage Modes and Capacity in Subnanometer Pores. *J. Phys. Chem. Lett.* **2012**, *3*, 1732−1737.
(11) Merlet, C.; Péan, C.; Rotenberg, B.; Madden, P. A.; Daffos, B.; Taberna, P.-L.; Simon, P.; Salanne, M. Highly Confined Ions Store Charge More Efficiently in Supercapacitors. *Nat. Commun.* **2013**, *4*, 2701.
(12) Ohba, T.; Hata, K.; Chaban, V. V. Nanocrystallization of Imidazolium Ionic Liquid in Carbon Nanotubes. *J. Phys. Chem. C* **2015**, *119*, 28424−28429.
(13) Chen, S.; Wu, G.; Sha, M.; Huang, S. Transition of Ionic Liquid [bmim][PF6] from Liquid to High-Melting-Point Crystal When Confined in Carbon Nanotubes. *J. Am. Chem. Soc.* **2007**, *129*, 2416−2417.
(14) Shim, Y.; Kim, H. J. Nanoporous Carbon Supercapacitors in an Ionic Liquid: A Computer Simulation Study. *ACS Nano* **2010**, *4*, 2345−2355.
(15) Lee, A. A.; Kondrat, S.; Kornyshev, A. A. Single-File Charge Storage in Conducting Nanopores. *Phys. Rev. Lett.* **2014**, *113*, 1−5.
(16) Rochester, C. C.; Kondrat, S.; Pruessner, G.; Kornyshev, A. A. Charging Ultrananoporous Electrodes with Size-Asymmetric Ions Assisted by Apolar Solvent. *J. Phys. Chem. C* **2016**, *120*, 16042−16050.
(17) Spohr, H. V.; Patey, G. N. Structural and Dynamical Properties of Ionic Liquids: Competing Influences of Molecular Properties. *J. Chem. Phys.* **2010**, *132*, 154504.
(18) Perkin, S. Ionic Liquids in Confined Geometries. *Phys. Chem. Chem. Phys.* **2012**, *14*, 5052.
(19) Kondrat, S.; Wu, P.; Qiao, R.; Kornyshev, A. A. Accelerating Charging Dynamics in Subnanometre Pores. *Nat. Mater.* **2014**, *13*, 387−393.
(20) He, Y.; Qiao, R.; Vatamanu, J.; Borodin, O.; Bedrov, D.; Huang, J.; Sumpter, B. G. The Importance of Ion Packing on the Dynamics of Ionic Liquids during Micropore Charging. *J. Phys. Chem. Lett.* **2016**, *7*, 36−42.
(21) He, Y.; Huang, J.; Sumpter, B. G.; Kornyshev, A. A.; Qiao, R. Dynamic Charge Storage in Ionic Liquids-Filled Nanopores: Insight from a Computational Cyclic Voltammetry Study. *J. Phys. Chem. Lett.* **2015**, *6*, 22−30.
(22) Tsai, W.-Y.; Taberna, P.-L.; Simon, P. Electrochemical Quartz Crystal Microbalance (EQCM) Study of Ion Dynamics in Nanoporous Carbons. *J. Am. Chem. Soc.* **2014**, *136*, 8722−8728.
(23) Griffin, J. M.; Forse, A. C.; Tsai, W.-Y.; Taberna, P.-L.; Simon, P.; Grey, C. P. In Situ NMR and Electrochemical Quartz Crystal Microbalance Techniques Reveal the Structure of the Electrical Double Layer in Supercapacitors. *Nat. Mater.* **2015**, *14*, 812−819.
(24) Rappe, A. K.; Goddard, W. A., III Charge Equilibration for Molecular Dynamics Simulations. *J. Phys. Chem.* **1991**, *95*, 3358−3363.
(25) Choudhury, A. R.; Winterton, N.; Steiner, A.; Cooper, A. I.; Johnson, K. A. In Situ Crystallization of Low-Melting Ionic Liquids. *J. Am. Chem. Soc.* **2005**, *127*, 16792−16793.
(26) Paek, E.; Pak, A. J.; Hwang, G. S. On the Influence of Polarization Effects in Predicting the Interfacial Structure and Capacitance of Graphene-like Electrodes in Ionic Liquids. *J. Chem. Phys.* **2015**, *142*, 024701.
(27) Paek, E.; Pak, A. J.; Hwang, G. S. A Computational Study of the Interfacial Structure and Capacitance of Graphene in [BMIM][PF6] Ionic Liquid. *J. Electrochem. Soc.* **2013**, *160*, A1−A10.
(28) Vatamanu, J.; Borodin, O.; Smith, G. D. Molecular Insights into the Potential and Temperature Dependences of the Differential Capacitance of a Room-Temperature Ionic Liquid at Graphite Electrodes. *J. Am. Chem. Soc.* **2010**, *132*, 14825−14833.
(29) Georgi, N.; Kornyshev, A. A.; Fedorov, M. V. The Anatomy of the Double Layer and Capacitance in Ionic Liquids with Anisotropic Ions: Electrostriction vs. Lattice Saturation. *J. Electroanal. Chem.* **2010**, *649*, 261−267.
(30) A Savitzky−Golay filter over a 2.5 ps trajectory window was used: Savitzky, A.; Golay, M. Smoothing and Differentiation of Data by Simplified Least Squares Procedures. *Anal. Chem.* **1964**, *36*, 1627−1639.
(31) Paek, E.; Pak, A. J.; Kweon, K. E.; Hwang, G. S. On the Origin of the Enhanced Supercapacitor Performance of Nitrogen-Doped Graphene. *J. Phys. Chem. C* **2013**, *117*, 5610−5616.
(32) Pak, A. J.; Paek, E.; Hwang, G. S. Impact of Graphene Edges on Enhancing the Performance of Electrochemical Double Layer Capacitors. *J. Phys. Chem. C* **2014**, *118*, 21770−21777.
(33) Pak, A. J.; Hwang, G. S. On the Importance of Regulating Hydroxyl Coverage on the Basal Plane of Graphene Oxide for Supercapacitors. *ChemElectroChem.* **2016**, *3*, 741−748.
(34) Plimpton, S. Fast Parallel Algorithms for Short-Range Molecular Dynamics. *J. Comput. Phys.* **1995**, *117*, 1−19.
(35) Daily, J. W.; Micci, M. M. Ionic Velocities in an Ionic Liquid under High Electric Fields Using All-Atom and Coarse-Grained Force Field Molecular Dynamics. *J. Chem. Phys.* **2009**, *131*, 094501.
(36) Roy, D.; Maroncelli, M. An Improved Four-Site Ionic Liquid Model. *J. Phys. Chem. B* **2010**, *114*, 12629−12631.
(37) Wang, Y.; Izvekov, S.; Yan, T.; Voth, G. A. Multiscale Coarse-Graining of Ionic Liquids. *J. Phys. Chem. B* **2006**, *110*, 3564−3575.
(38) Jorgensen, W. L.; Maxwell, D. S.; Tirado-Rives, J. Development and Testing of the OPLS All-Atom Force Field on Conformational Energetics and Properties of Organic Liquids. *J. Am. Chem. Soc.* **1996**, *118*, 11225−11236.
(39) Deserno, M.; Holm, C. How to Mesh up Ewald Sums. I. A Theoretical and Numerical Comparison of Various Particle Mesh Routines. *J. Chem. Phys.* **1998**, *109*, 7678−7693.
(40) Toukmaji, A. Y.; Board, J. A. Ewald Summation Techniques in Perspective: A Survey. *Comput. Phys. Commun.* **1996**, *95*, 73−92.
(41) Lopes, N. C.; Deschamps, J.; Pádua, A. A. H. Modeling Ionic Liquids Using a Systematic All-Atom Force Field. *J. Phys. Chem. B* **2004**, *108*, 2038−2047.
(42) de Andrade, J.; Böes, E. S.; Stassen, H. Computational Study of Room Temperature Molten Salts Composed by 1-Alkyl-3-Methyl-imidazolium Cations − Force-Field Proposal and Validation. *J. Phys. Chem. B* **2002**, *106*, 13344−13351.
(43) van Duin, A. C. T.; Dasgupta, S.; Lorant, F.; Goddard, W. A. ReaxFF: A Reactive Force Field for Hydrocarbons. *J. Phys. Chem. A* **2001**, *105*, 9396−9409.
(44) Nakano, A. Parallel Multilevel Preconditioned Conjugate-Gradient Approach to Variable-Charge Molecular Dynamics. *Comput. Phys. Commun.* **1997**, *104*, 59−69.
(45) Chenoweth, K.; van Duin, A. C. T.; Goddard, W. A. ReaxFF Reactive Force Field for Molecular Dynamics Simulations of Hydrocarbon Oxidation. *J. Phys. Chem. A* **2008**, *112*, 1040−1053.
(46) Hoover, W. Canonical Dynamics: Equilibrium Phase-Space Distributions. *Phys. Rev. A: At., Mol., Opt. Phys.* **1985**, *31*, 1695−1697.

DOI: 10.1021/acs.jpcc.6b06637
J. Phys. Chem. C 2016, 120, 24560−24567